

Capabilities of X-ray diffuse scattering method for study of microdefects in semiconductor crystals

Vladimir T. Bublik¹, Marina I. Voronova¹, Kirill D. Shcherbachev¹

1 National University of Science and Technology (MISiS), 4 Leninsky Prospekt, Moscow 119049, Russia

Corresponding author: Kirill D. Shcherbachev (shcherbachev.kirill@mail.ru)

Received 17 August 2018 ♦ Accepted 5 October 2018 ♦ Published 1 December 2018

Citation: Bublik VT, Voronova MI, Shcherbachev KD (2018) Capabilities of X-ray diffuse scattering method for study of microdefects in semiconductor crystals. *Modern Electronic Materials* 4(4): 125–134. <https://doi.org/10.3897/j.moem.4.4.47197>

Abstract

The capabilities of X-ray diffuse scattering (XRDS) method for the study of microdefects in semiconductor crystals have been overviewed. Analysis of the results has shown that the XRDS method is a highly sensitive and information valuable tool for studying early stages of solid solution decomposition in semiconductors. A review of the results relating to the methodological aspect has shown that the most consistent approach is a combination of XRDS with precision lattice parameter measurements. It allows one to detect decomposition stages that cannot be visualized using transmission electron microscopy (TEM) and moreover to draw conclusions as to microdefect formation mechanisms. TEM-invisible defects that are coherent with the matrix and have smeared boundaries with low displacement field gradients may form due to transmutation doping as a result of neutron irradiation and relaxation of disordered regions accompanied by redistribution of point defects and annihilation of interstitial defects and vacancies. For GaP and InP examples, a structural microdefect formation mechanism has been revealed associated with the interaction of defects forming during the decomposition and residual intrinsic defects. Analysis of XRDS intensity distribution around the reciprocal lattice site and the related evolution of lattice constant allows detecting different decomposition stages: first, the formation of a solution of Frenkel pairs in which concentration fluctuations develop, then the formation of matrix-coherent microdefects and finally coherency violation and the formation of defects with sharp boundaries. Fundamentally, the latter defects can be precipitating particles. Study of the evolution of diffuse scattering iso-intensity curves in GaP, GaAs(Si) and Si(O) has allowed tracing the evolution of microdefects from matrix-coherent ones to microdefects with smeared coherency resulting from microdefect growth during the decomposition of non-stoichiometric solid solutions heavily supersaturated with intrinsic (or impurity) components.

Keywords

microdefects, X-ray diffuse scattering, single crystals, semiconductors

1. Introduction

Among the problems faced by the technologies of semiconductor single crystals with preset properties that are determined mainly by the structural perfection and homogeneity of the crystals, there are important issues relating to the origins and properties of microdefects in

their crystal lattice as well as microdefect study and non-destructive control methods. Hereinafter we will consider microdefects to be local violations of crystal lattice periodicity caused by clusters of point defects (intrinsic or impurity), dislocation loops or dispersed phase precipitates having submicron or micron sizes. All these violations are first type defects [1] by their effect on X-ray diffrac-

tion. Various microdefect study methods were reviewed and their information value, advantages and drawbacks were discussed earlier [2]. The most information valuable one of these methods is X-ray diffuse scattering which allows analyzing the distribution of scattered X-ray waves in the vicinity of the reciprocal lattice site. XRDS measurement in triple-crystal X-ray diffractometer setup allows fundamental identification of microdefects and determination of their sizes and concentration. The theory of the method is continuously improved. Accurate analytical expressions were obtained [3] for the diffuse components of one-dimensional cross-sections and reciprocal space maps measured in Bragg diffraction setup for single crystals containing several types of defects. Analytical processing of experimental reflection curves and reciprocal space maps allowed determination of complex microdefect structures in silicon [4, 5] and garnet [6, 7] crystals exposed to radiation. The use of synchrotron sources greatly broadens the capabilities of the XRDS method. In ion implanted tungsten single crystals, this method revealed and allowed studying 3 nm radius dislocation loops of vacancy and interstitial type [8] which are almost irresolvable in transmission electron microscopy (TEM) images. The results obtained using XRDS and TEM for larger defects in metals are in good agreement.

Below we will dwell upon more detailed aspects of the problem in question: capabilities of the XRDS method paired with precision lattice parameter measurements on a diffractometer with a laboratory-grade X-ray source for the study of microdefects in semiconductor single crystals.

2. Theory

The theory of X-ray diffuse scattering (XRDS) from defects near Bragg reflections was put forward by Dederichs [10, 11] and Larson [12]. In this section, we will consider the theoretical basis of the method which will be required for further analysis of experimental data.

The XRDS intensity distribution $I(\mathbf{q})$ is determined by the Fourier image of the defect's displacement field $\mathbf{u}(\mathbf{q})$

$$I(\mathbf{q}) \sim |\mathbf{Q}\cdot\mathbf{u}(\mathbf{q})|^2, \quad (1)$$

where $\mathbf{q} = \mathbf{Q} - \mathbf{H}$ is the vector describing the deviation of the diffraction vector \mathbf{Q} from the reciprocal lattice site described by the vector \mathbf{H} .

If the local displacements around the defects are small and $\mathbf{Q}\cdot\mathbf{u}(\mathbf{q}) \ll 1$, the differential cross-section of diffuse scattering $S_{\text{dif}}(\mathbf{q})$ is written in the form [1, 13]

$$S_{\text{dif}}(\mathbf{q}) = N|F_H|^2 \left[\frac{H^2 C^2}{q^2} \sum_1^3 \pi_i \gamma_i + \frac{(HC)^2}{v_0^2 q} \sqrt{\pi_1 \gamma_1} \right], \quad (2)$$

where F_H is the structural amplitude, N is the number of scattering centers, C is the defect power that characterizes the crystal volume change ΔV caused by the defect and,

for a specific microdefect type, can be expressed through defect parameters (shape, size and deformation sign), and v_0 is the unit cell volume. For example, a defect with a Coulomb type displacement field $\mathbf{u}(\mathbf{r}) \gg \mathbf{C}(\mathbf{r}_0)/r^2$ has the power $\mathbf{C}(\mathbf{r}_0)$ which depends on the direction of the unit vector \mathbf{r}_0 and its sign is similar to that of ΔV . If $\Delta V > 0$, then $C > 0$ too, and vice versa. The parameters π_i and γ_i are determined (see e.g. [1]) as follows:

$$\begin{aligned} \pi_1 &= \frac{(\text{Tr}P_{mn})}{3}; \\ \pi_2 &= \sum_{n \rightarrow m} \frac{P_{nm} - P_{mm}}{6}; \\ \pi_3 &= 2 \sum_{n > m} \frac{(P_{mn})^2}{3}, \end{aligned} \quad (3)$$

where $\text{Tr}P_{mn}$ is the trace of the double-force tensor P_{mn} . The factors γ_i depend on the elastic constants of the material and the directions of the vectors \mathbf{q} and \mathbf{H} . For high-symmetry directions of \mathbf{q} and \mathbf{H} in cubic crystals, e.g., for 100, 110 and 111 type sites, the γ_i expressions are relatively simple (see, table 8 [1]). For specific defect symmetries, some of the parameters π_i take on zero. For cubic symmetry defects only the parameter π_1 differs from zero, for tetragonal symmetry $\pi_3 = 0$ and for trigonal symmetry $\pi_2 = 0$. In some cases, $\gamma_i = 0$; thus choosing the directions of \mathbf{q} and \mathbf{H} one can separately determine π_i and thence the symmetry of the defect's displacement field.

During point defect association in the course of structural transformation caused by post-crystallization cooling and process heat treatments, the sizes of the strong distortion regions around defects increase. As a result, the range of q for which the relationship $I(q) \sim q^{-2}$ is true (the Huang scattering region) is narrowed. For heavily distorted regions ($\mathbf{Q}\cdot\mathbf{u}(q) \gg 1$) the diffuse scattering intensity is described by the Stokes–Wilson asymptotic approximation ($S_{\text{dif}}^{\text{ADS}}(q)$). In the $q \gg q_0(QC)^{-1/2}$ range the asymptotic diffuse scattering cross-section expression takes on as follows [1]:

$$S_{\text{dif}}^{\text{ADS}}(q) = N|F_H|^2 \frac{CH}{v_0 q^4} \Psi\left(\frac{\mathbf{H}}{H}, \frac{\mathbf{q}}{q}\right); \quad (4)$$

here the function $\Psi \sim 2$ depends on the angle between the vectors \mathbf{H} and \mathbf{q} .

The components of the tensor P_{mn} for dislocation loops are described as follows:

$$P_{mn} = (C_{12} \text{Tr}\Omega_{mn} + \Omega_{m}d)\delta_{nm} + 2C_{44}\Omega_{nm}, \quad (5)$$

where $\Omega_{mn} = 0.5(F_n b_m + F_m b_n)$, $d = C_{11} + C_{12} + 2C_{44}$; C_{ij} are the components of the elasticity tensor for the cubic symmetry crystal; \mathbf{F} and \mathbf{b} are the vector characterizing the dislocation loop plane and its Burgers vector, respectively.

The first term in brackets of Eq. (2) corresponds to Huang scattering $S_{\text{dif}}^H(q)$ which is symmetrical relative

to the reciprocal lattice site ($q = 0$). The second term characterizes the asymmetrical part of the diffuse scattering intensity $S_{\text{dif}}^A(q)$ and the shift of the diffuse scattering intensity distribution towards positive (at $\Delta V > 0$) or negative (at $\Delta V < 0$) q_z (q_z is the projection of the vector \mathbf{q} parallel to the reciprocal lattice vector). The XRDS intensity near reciprocal lattice sites can be conveniently represented in the form of equal intensity surfaces (iso-intensity curves) or their sections by the diffraction plane. In the Huang scattering region at small q the equation of the diffuse scattering iso-intensity contours is

$$q^2 = \text{const} \sum_{i=1}^3 \pi_i \gamma_i.$$

The shape of the diffuse scattering iso-intensity contours is determined by the type of the defects and the symmetry of their displacement fields. The shape of the diffuse scattering iso-intensity curves allows one to determine the symmetry of the displacement field and choose between their possible configurations. It is sometimes sufficient to analyze the XRDS intensity distribution along with directions parallel or perpendicular to the reciprocal lattice vector of the respective site. With an increase in q length the experimental dependences should exhibit changes in the law of XRDS intensity decrease. One can separate three q regions:

- Huang scattering region: scattering at weak elastic lattice distortions far from the defect centre. The distance r from the defect centre is far greater than its characteristic size R_0 . The intensity expression is $I(q) \sim q^{-2}$. The tangent of the slope angle of the $\lg I(q) = f(\lg q)$ dependence in this region is -2;
- asymptotic diffuse scattering (ADS) region: scattering at relatively strong lattice distortions obeying the elastic continuum theory. In this case $I(q) \sim q^{-4}$, which corresponds to a slope of -4 (in the same coordinates). The bending point q_0 , which marks the Huang to asymptotic scattering transition can be used for evaluating the defect's power:

$$q_0 = \frac{1}{\sqrt{HC}}; \quad (6)$$

- defect core scattering region. This is the region of small $r \leq R_0$ (Laue scattering) in which scattering is quite difficult for experimental measurement since at low defect concentrations and sufficiently large $q > q_T$ even Laue scattering is but a small part of the thermal diffuse scattering which decreases in the same coordinates with a slope of -2. This scattering can be used as the internal reference for defect concentration determination [14].

The expression of diffuse scattering at thermal oscillations [15] is as follows:

$$S_{\text{dif}}^T = N |F_H|^2 \frac{kTH^2}{v_0 q^2} K(\mathbf{Q}, \mathbf{q})$$

where $K(\mathbf{Q}, \mathbf{q})$ is the Christoffel determinant that depends on the directions of the vectors \mathbf{Q} and \mathbf{q} [15].

A convenient expression was reported [14] for assessing the concentration n_{def} of microdefects in the crystal from the ratio of the Huang and thermal diffuse scattering intensities:

$$\frac{S^H(q_H)}{S^T(q_T)} = \frac{n_{\text{d.f.}}(C)^2 |q_T|^2}{kT |q_H|^2} \frac{\Psi(\mathbf{Q}, \mathbf{q})}{K(\mathbf{Q}, \mathbf{q})}, \quad (7)$$

where q_H, q_T are the wave vectors for the angular deviations from the reciprocal lattice site where Huang or thermal diffuse scattering dominate.

This expression allows measuring the XRDS intensity from microdefects in absolute units without allowance for the scattering layer volume, the structural amplitude, the Debye-Waller factor and the solid scattering angle. Thus such parameters as the symmetry, volume and concentration of the microdefects can be determined directly from the experimental data on the diffuse scattering intensity for the test crystal.

The above q dependences of differential scattering cross-sections are somewhat different from the experimental intensity vs q dependences. To provide for the required light power when a synchrotron radiation source is used, one has to impart a certain vertical divergence to the beams (this divergence is perpendicular to the diffraction plane). In this case the slopes of the XRDS intensity vs q dependences $I(q)$ are not -2 and -4, but -1 and -3, respectively.

Huang scattering is efficient if all the microdefects have the same sign of power C . However, if the test crystal contains microdefects with different power signs, i.e., vacancy and interstitial type microdefects are present, and especially if there are microdefects smaller than ~ 1 nm in size, the asymptotic scattering region is more experimentally accessible. In this region the vectors \mathbf{q} satisfy the condition $(CQ)^{-0.5} \ll q \ll CQR_0^{-3}$, where R_0 is the characteristic microdefect size [1]. Hence an increase in the power of microdefects makes the left-hand part of this expression so small (the Huang scattering region) that to become experimentally inaccessible since it becomes smaller than the instrumentally detectable size of reciprocal lattice site. In this case, microdefect power information can be obtained from ADS analysis. Due to the inverse symmetry of the displacement field in the crystal, one can always find points that are equidistant from the defect centre in which the local lattice distortion is the same and which therefore reflect radiation to the same reciprocal space point. The interference of the radiation reflected by these regions produces oscillations at one side of the reciprocal lattice site depending on the defect power sign. Plotting the asymptotic scattering dependence along the q axis as $I(q_z)q_z^3$ vs q_z , one can clearly see these oscillations and use their period for evaluating the power of the defects even if the crystal contains both vacancy and interstitial type defects, because oscillations of radiation scattered by these defects are located at opposite

sides of the reciprocal lattice site (at $q_z < 0$ and at $q_z > 0$, respectively) [17]. The power of the microdefects can be assessed from the distance between two adjacent maxima:

$$C = \frac{1}{H(q_z^{2/3} - q_{z_1}^{2/3})^3}, \quad (8)$$

where q_{z_i} ($i = 1, 2$) are the coordinates of the two adjacent maxima in the $Iq_z^3 = f(q_z)$ dependence. The number of maxima in the region $(CQ)^{0.5} \ll q \ll (CQ)R_0^{-3}$ is as follows [18]:

- for dislocation loops:

$$n_L = Qb_L, \quad (9)$$

where b_L is the Burgers vector of the loop;

- for defect clusters with the radius R_{cl} :

$$n_{cl} = \frac{4}{3}\pi QR_{cl}.$$

Thus, the XRDS intensity is determined by the double-force tensor components. However, the actually measured XRDS intensity is that for the near region of the reciprocal lattice sites. Clearly, this situation refers to defects far greater than the atomic sizes. The use of synchrotron sources and low temperature for experiments allow studying displacement fields for discrete point defects by measuring XRDS intensity distribution over the entire Brillouin zone around the reciprocal lattice site, when the intensity is low or (at low defect concentrations) even lower than the room temperature thermal diffuse scattering intensity.

On the other hand, a change in the lattice parameter caused by point defects in the crystal is also related to the double-force tensor components. For example, in cubic crystals [1] the relative change in the lattice parameter $\Delta a/a$ caused by point defects with concentration n is

$$3\frac{\Delta a}{a} = n\frac{\Delta V}{V} = \frac{n\sqrt{3\pi_1}}{v_0(C_{11} + 2C_{12})}, \quad (10)$$

where $\Delta V/V$ is the relative change in the crystal volume caused by one defect and C_{ij} are the elastic moduli. If point defects produce a displacement field with a cubic symmetry, then $P_{11} = P_{22} = P_{33}$ and $\pi_1 = 3P_{11}^2$, whence

$$3\frac{\Delta a}{a} = -\frac{3n\pi_1}{v_0(C_{11} + 2C_{12})}, \quad (11)$$

where

$$P_{11} = (C_{11} + 2C_{12})v_0\frac{\Delta r}{r}. \quad (12)$$

Equations (11) and (12) give the relaxation volume for one point defect which can be evaluated from the respective change in the lattice parameter:

$$3n^{-1}\frac{\Delta a}{a} = 3\frac{\Delta r}{r}, \quad (13)$$

where $\Delta r/r$ is the relative difference in the atomic radii of the matrix and the point defect. If the lattice contains point defects with positive and negative Δr , then the overall change $\Delta a/a$ will be the superposition of these solid solutions:

$$3\frac{\Delta a}{a} = \frac{1}{v_0(C_{11} + 2C_{12})} [n_i \text{Tr}(P_{ij}^i) - n_v \text{Tr}(P_{ij}^v)], \quad (14)$$

where n_i, n_v are the concentrations of interstitial and vacancy type defects.

Thus, precision lattice parameter measurements allow evaluating the differential point defect concentration if the relaxation volumes are known. The symmetrical part of Huang scattering does not depend on the defect power sign, and the intensities of the radiation scattered from defects with opposite power signs are superimposed. However, at somewhat greater q for which the asymptotic approximation is valid (see Eq. (4)), $I_{\text{diff}}^{\text{ADS}} \sim \Delta V/q^4$; here ΔV is the volume change per one defect. As a result, the scattering intensity for vacancy and interstitial type defects is distributed at different sides of the reciprocal lattice site.

Thus, precision lattice parameter and diffuse scattering measurements are complementary methods allowing one to analyze structural changes in the state of point defects at early stages of solid solution decomposition in semiconductors. We will demonstrate this below with some examples.

3. Experimental

3.1 Oxygen solid solution in silicon

Early precipitation stages in Si(O) solid solution containing $(7-8) \cdot 10^{17} \text{ cm}^{-3}$ oxygen in silicon was studied [14]. XRDS intensity measurements near the $[[400]]$ site in crystals after homogenization annealing at 1000 °C showed that this intensity was close to the detection limit against the thermal scattering intensity background. However, the XRDS intensity grew by almost three orders of magnitude after annealing at 450 °C. The shape of the diffuse scattering iso-intensity curve shown in Fig. 1 indicates that the microdefects which form as a result of annealing and scatter near the reciprocal lattice site were coherent with the matrix and have planar shapes. The shift of the iso-intensity curve section towards positive vectors q from the reciprocal lattice site suggests that the microdefect power sign was positive ($C > 0$). Note that these microdefects are not detectable by transmission electron microscopy (TEM) or metallographic methods since they are coherent with the matrix and have smeared boundaries

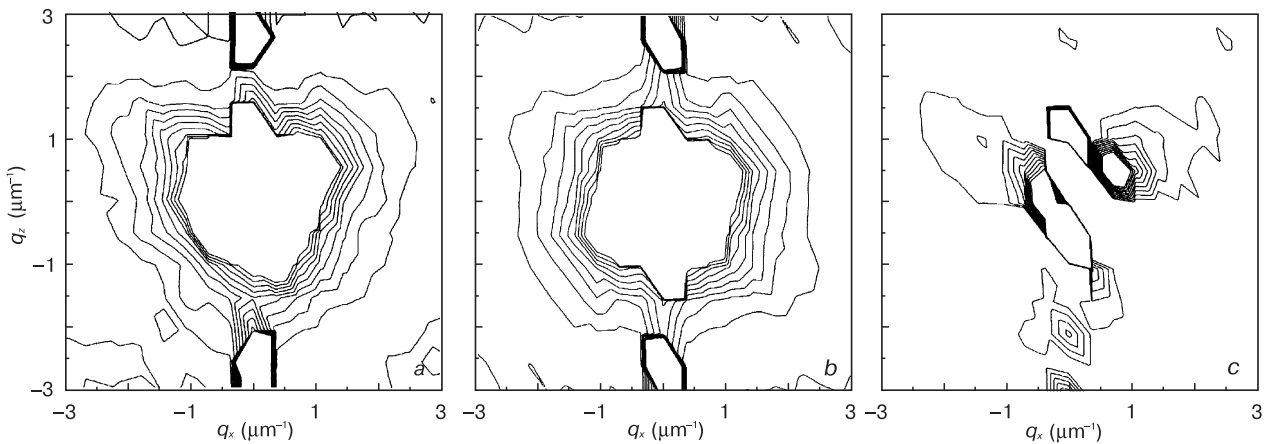


Figure 1. XRDS scattering intensity distribution near the $[[400]]$ site for silicon single crystal after homogenizing annealing at $1000\text{ }^{\circ}\text{C}$ and annealing at $450\text{ }^{\circ}\text{C}$ (16 h): (a) experimental iso-intensity curve, (b) symmetrical component and (c) asymmetrical component. XRDS intensity for the iso-intensity curves varies in the 0.5–9.5 cps range with a 1.0 cps step.

where the deformation gradient is insufficient to produce contrast in TEM images. However, this process was reported to cause hardening of Si crystals [19].

3.2 Indium antimonide neutron irradiation

TEM-undetectable defects that are coherent with the matrix and have smeared boundaries with small displacement field gradients can also be produced by neutron irradiation and relaxation of disordered regions accompanied by redistribution of point defects and annihilation of interstitial and vacancy type defects. The dependence of the increase in the indium antimonide lattice parameter on the neutron fluence showed that, according to calculations, only ~ 20 Frenkel pairs out of 600 per one fast reactor neutron ($E > 0.1\text{ MeV}$) remained after annihilation [20], which is far smaller than for other A^3B^5 compounds (e.g. 100 Frenkel pairs per one neutron remained after GaAs irradiation in the same reactor). However, the vacancy and interstitial type defects remaining in InSb agglomerated into vacancy and interstitial type microdefects. Fig. 2 shows a change in the XRDS intensity along q_z . Judging from the positions of the bending points for positive and negative q_z , the $I_{\text{diff}}(q)q^3 = f(q)$ dependences for the initial crystals suggest that the InSb crystals before irradiation had local inhomogeneities of both vacancy (V–MD) and interstitial (I–MD) types with sizes of ~ 0.45 and 0.5 nm , respectively. The XRDS intensity for $q_z > 0$ was somewhat higher (the overall volume of V–MD is greater by about 10%), with the microdefects being mainly non-spherical in shape [20]. Neutron irradiation at higher fluencies showed that the scattering pattern changed noticeably at fluencies of $\sim 5 \times 10^{16}\text{ cm}^{-2}$. The XRDS intensity decreased dramatically for $q_z < 0$ and somewhat increased for $q_z > 0$. Obviously, the sizes and number of non-spherical V–MD decrease. After annealing of these crystals, integrated analysis of the change in the lattice parameter, carrier concentrations as determined from the number of Sn atoms occupying In sites as a result of transmutation, and XRDS

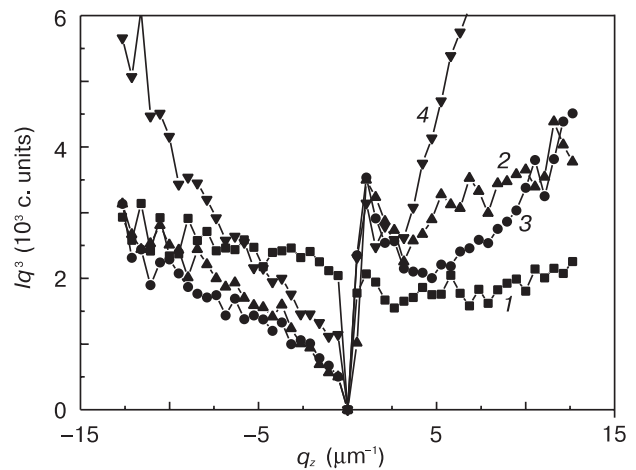


Figure 2. XRDS scattering intensity distribution along the q_z cross-section of the diffuse scattering iso-intensity curve for the $[[224]]$ site of fast neutron irradiated InSb crystals at different fluencies ϕ_p , cm^{-2} : (1) initial crystal; (2) fluence $5 \times 10^{16}\text{ cm}^{-2}$; (3) $5 \times 10^{17}\text{ cm}^{-2}$; (4) $1.3 \times 10^{18}\text{ cm}^{-2}$.

intensity (see e.g. Fig. 3) allows tracing the structural evolution regularities during annealing. For example, annealing at below $200\text{ }^{\circ}\text{C}$ caused a significant change in the XRDS intensity distribution, the lattice parameter remaining the same. Radiation defect annihilation and hence a decrease in the lattice parameter only began at a $300\text{ }^{\circ}\text{C}$ annealing temperature. One can conclude [21] that the annihilation activation energy is higher than the self-diffusion activation energy.

3.3 Indium phosphide neutron irradiation

An interesting example demonstrating the efficiency of combined lattice parameter and XRDS measurements is a study of InP crystal structure after transmutation doping by reactor neutron irradiation [22, 23]. The data shown in Fig. 4 suggest two factors that influence the lattice parameter. One is the increase in the lattice parameter due

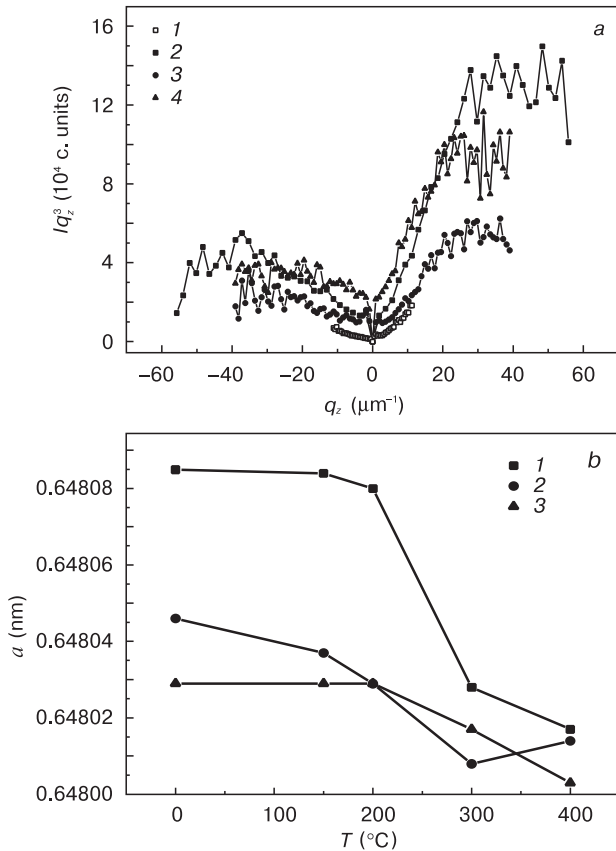


Figure 3. (a) XRDS scattering intensity distribution along the q_z cross-section of reciprocal space for fast neutron irradiated InSb(Te) crystal at $1.3 \cdot 10^{18} \text{ cm}^{-2}$ fluence (1) before and (2) after heat treatment at different temperatures and (b) lattice parameter of InSb single crystals with different initial carrier concentration irradiated with neutrons at different fluencies F as a function of subsequent heat treatment temperature: (a) (1) before heat treatment, (2) after heat treatment at 150°C , (3) at 200°C and (4) at 300°C ; (b) (1) InSb(Te), $n_0 = 4 \cdot 10^{14} \text{ cm}^{-3}$, $F_{fn} = 1.3 \cdot 10^{18} \text{ cm}^{-2}$; (2) InSb(Mn), $p_0 = 5 \cdot 10^{13} \text{ cm}^{-3}$, $F_{fn} = 5 \cdot 10^{17} \text{ cm}^{-2}$; (3) InSb(Te), $n_0 = 1.7 \cdot 10^{15} \text{ cm}^{-3}$, $F_{sn} = 4.3 \cdot 10^{17} \text{ cm}^{-2}$.

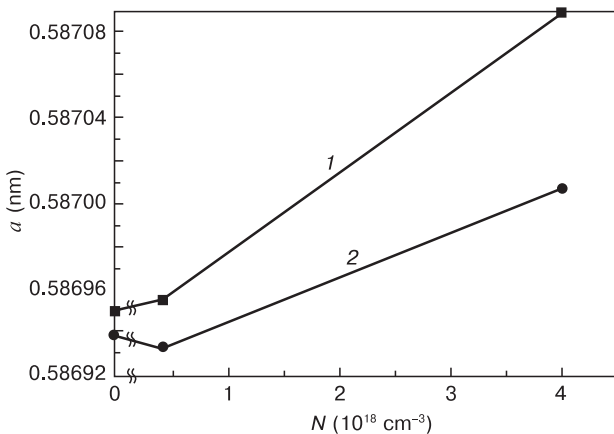


Figure 4. InP lattice parameter as a function of major carrier concentration (1) before and (2) after neutron irradiation at $2.3 \cdot 10^{19} \text{ cm}^{-2}$ fluence (thermal and rapid neutron fluence ratio is 1).

to tellurium doping (with part of Te being electrically inactive due to the formation of In_2Te_3 complexes which do not form microdefects as suggested by the low diffuse scattering intensity). A similar observation was made later using the same methods for GaP single crystals that were also doped with a 6B subgroup element (sulfur). InP neutron irradiation decreased the lattice parameter over the entire Te concentration range. This decrease was for the first time revealed for InP and for single crystals irradiated with different neutron fluencies (Fig. 5). It was shown [22, 23] that experimental lattice parameter and XRDS measurement results can be accounted for in the assumption that antisite defects P_{In} (phosphorus in indium position) form in the crystal in a sufficient quantity to decrease the lattice parameter in the presence of Frenkel defects which increase the lattice parameter. The crystals were heat-treated [23] for checking this model. The effect of anneals on the lattice parameter and XRDS distribution suggested the validity of the above defect formation model for InP. Figure 6 shows that for annealing at up to approx. 500°C the increase in the lattice parameter was in agreement with the concentration of the antisite defects, which is $\sim 5 \cdot 10^{18} \text{ cm}^{-3}$. However, the change in the XRDS distribution pattern during the anneals [23] suggested that the process was more complex. The XRDS intensity distribution pattern shown in Fig. 6 b suggests that e.g. the 300°C annealing caused not only recombination of antisite defects (transfer of P atoms from In positions to phosphorus vacancies), i.e., a process that increases the lattice parameter, but also recombination of vacancy and interstitial type defects associated into microdefects due to the migration of interstitial defects towards V-MD and vacancies towards I-MD. These microdefects are matrix-coherent concentration fluctuations of vacancy and interstitial type point defects. Obviously, this process should decrease the lattice parameter and therefore the experimentally observed growth in the lattice parameter suggests that the actual concentration of

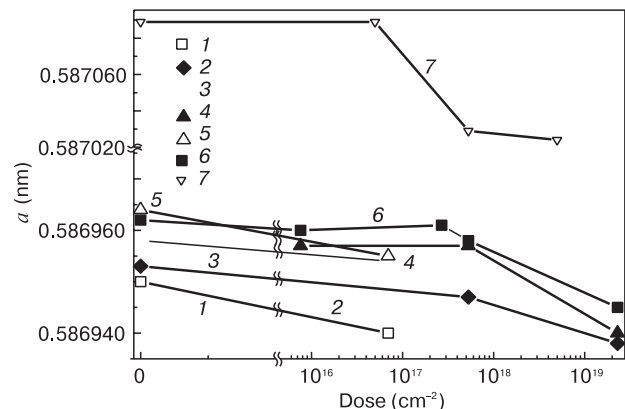


Figure 5. InP lattice parameter as a function of rapid neutron fluence for crystals with different initial impurity content n , cm^{-3} : (1) major carrier concentration $(1.6\text{--}2.3) \cdot 10^{18}$; (2) $3.5 \cdot 10^{16}$; (3) $(3\text{--}4.1) \cdot 10^{16}$; (4) $2 \cdot 10^{17}$; (5) $(4.2\text{--}5.2) \cdot 10^{16}$; (6) $8 \cdot 10^{17}$; (7) $3.9 \cdot 10^{18}$.

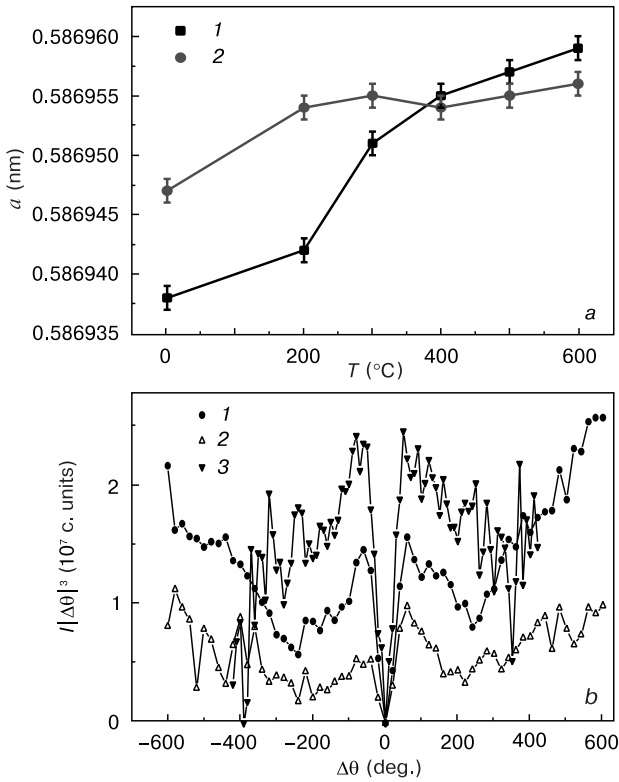


Figure 6. (a) lattice parameter and (b) XRD intensity for InP specimen as a function of Bragg angle deviation at different annealing temperatures: (a) (1) fluence $2.3 \cdot 10^{19} \text{ cm}^{-2}$; (2) $5.3 \cdot 10^{17} \text{ cm}^{-2}$; (b) fluence $2.3 \cdot 10^{19} \text{ cm}^{-2}$: (1) $T_{\text{ann}} = 200 \text{ }^\circ\text{C}$; (2) 300; (3) 500.

antisite defects was higher than the above estimate. The energy barrier of recombination, in this case, seems to be lower than for microdefects with sharp boundaries (dislocation loops or precipitates). Thus most antisite defects were annealed at $\sim 500 \text{ }^\circ\text{C}$. At the same time, since the lattice parameter did not change anymore upon $500 \text{ }^\circ\text{C}$ annealing and the XRD intensity grew dramatically, but the intensity curve bending points remained almost at the same positions, it is safe to assume that the predominant process at this temperature was point defect redistribution causing an increase in the overall volume of large (about 1 mm) microdefects.

3.4 Nonstoichiometric gallium phosphide and arsenide crystals

We consider another typical application example of the methods. Post-growth cooling of nonstoichiometric GaAs and GaP crystals with significant quantities of excess cations caused precipitation of excess Ga resulting in the formation of interstitial Ga (Ga_i) and Ga_i complexes with residual interstitial phosphorus atoms (P_i) [24]. The subsequent decomposition stages involved defect complexes agglomeration into matrix-coherent microdefects, their growth in size or increasing quantity and finally, violation of microdefect coherency with the matrix due to elastic stress relaxation around the microdefects. We consider experimental results for undoped GaP single crystals. The lattice parameter of the wafers cut from the beginning of the ingots was $0.545133\text{--}0.545130 \text{ nm}$ (the stoichiometric GaP lattice parameter is 0.545514 nm). The somewhat increase in the lattice parameter to 0.545137 nm for wafers cut from the end of the ingot was caused by intense gallium precipitation and the formation of XRDS-detectable microdefects. Fig. 7 a shows XRDS intensity distribution for the specimen containing $\sim 4 \times 10^{18} \text{ cm}^{-3}$ phosphorus vacancies. It can be seen from Fig. 7 a that the XRDS intensity was low, and the typical iso-intensity contours suggests that the scattering was at plate-like matrix-coherent microdefects. The shift of the iso-intensity contours center of gravity toward $q_z > 0$ suggests that the microdefects had a positive power. Fig. 7 b shows the iso-intensity contours for a largely nonstoichiometric specimen. The iso-intensity curve pattern is the same as for the previous example, but the higher intensity suggests that the total volume of the matrix-coherent microdefects was considerably larger. Fig. 8 a shows the q_x cross-section of the iso-intensity contours for the two above specimens. Their intensities differ by approximately one order of magnitude, and hence the total volume of the microdefects differ by one order of magnitude also.

Fig. 7 c shows the iso-intensity contours for the specimen in which the decomposition caused somewhat increase in the lattice parameter. It can be seen (Fig. 7 c)

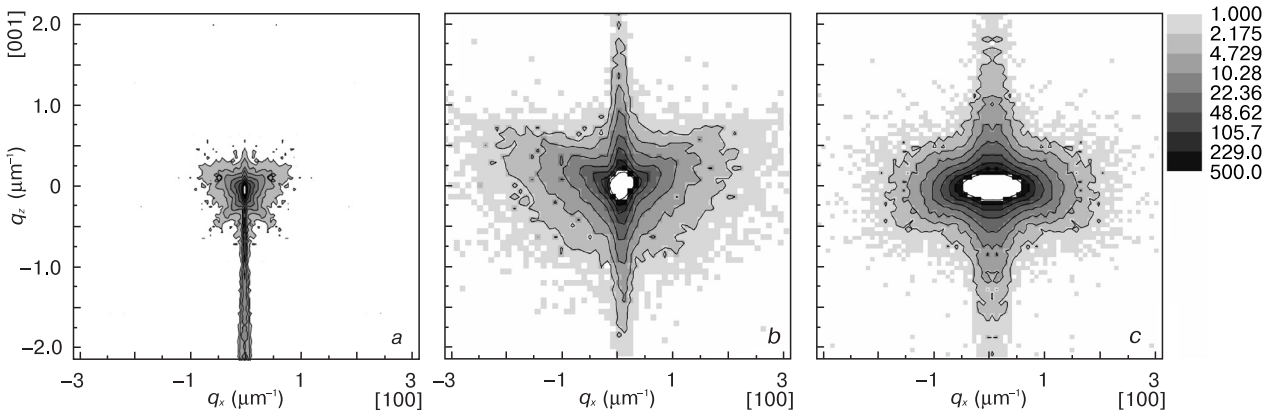


Figure 7. Typical XRDS scattering intensity distribution for GaP and GaAs crystals grown from Ga excess melt: (a) ingot beginning, (b) middle and (c) end.

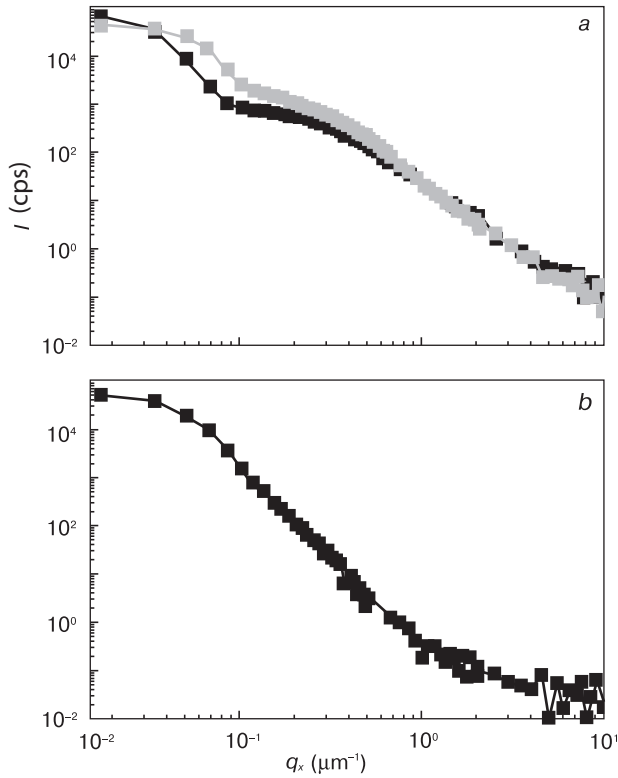


Figure 8. XRDS scattering intensity distribution along q_x cross-section: (a) ingot beginning and (b) end.

that the intensity distribution near the site was quite symmetrical. Thus the microdefect sizes were sufficient for stress relaxation around the microdefects. The shape of the q_x cross-section (Fig. 8 b) suggests that the increase in the XRDS intensity was accompanied by an increase in the curve slope. In the working range for which the asymptotic approximation is valid, the curve slopes may exceed -3 if the vector q_x is even greater than for the asymptotic approximation region [1] which may be true if the microdefects are large enough.

Thus, analysis of the XRDS pattern shown in Figs 7 and 8 and the lattice parameter evolution suggests different decomposition stages: first the formation of a solution of Frenkel defects in which concentration fluctuations develop (see above), then the formation of matrix-coherent microdefects and finally coherency violation and the formation of defects with sharp boundaries which may be precipitating particles. A similar observation was made earlier [25] for the decomposition of oxygen solid solution in silicon.

3.5 Formation of dislocation loops in nonequilibrium solid solutions

We consider another interesting XRDS method application: a study of dislocation loops forming at a certain stage of point defect structural state evolution in nonequilibrium solid solutions. Dislocation loops are described by their strength (diameter and Burgers vector) and planes.

Typically the loop plane and its Burgers vector are determined by comparing the calculated and experimental diffuse scattering iso-intensity curves. If the loops have a homogeneous size distribution, their linear parameters can be determined using two methods. The average loop radius R_0 can be evaluated from the vector q_0 corresponding to the knee point in the q_x cross-section of the diffuse scattering iso-intensity curve using the formula

$$R_0 = \left(H \pi b q_0^2 \right)^{-\frac{1}{2}},$$

where H is the diffraction vector and b is the Burgers vector.

The other method is based on analysis of the $I_{\text{diff}}(q_z)q_z^3 = f(q_z)$ dependence. Fig. 9 shows a plot of this dependence for two regions of the GaAs wafer measured in the vicinity of the $[[333]]$ site in the $[[111]]$ direction. The first region where $q_z > 0$ exhibited clear oscillations. In accordance with Eq. (9), their number is equal to the scalar product of the Burgers vector and the diffraction vector and is 3. The positions of the oscillations at $q_z > 0$ suggest that these loops are of an interstitial type. Since the scattering intensity at $q_z < 0$ is low, dislocation loops are probably the predominant defect type in this region. The power of the loops assessed from the oscillation period was $4 \times 10^{-4} \text{ mm}^3$, and so their radius was estimated to be $\sim 0.5 \text{ nm}$. This estimate agrees with the loop radius assessed from the q_0 value. (The respective figure is not shown for brevity.) The diffuse scattering pattern for the other region was completely different. The diffuse scattering intensity (the amplitude and period of the oscillation peaks) suggests that the number and sizes of the loops decreased. At the same time, intense scattering arose at $q_z < 0$, i.e., from defects with negative power the volume of which seems to be even greater than in the first region. The advantage of the XRDS method showed itself for this case in the higher statistical confidence of the results.

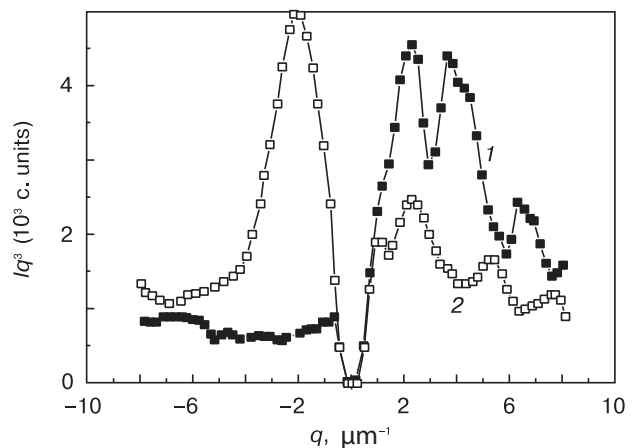


Figure 9. XRDS scattering intensity distribution along $q_z \parallel [[111]]$ direction for two points of GaAs(Si) specimen section ($n = 4.8 \cdot 10^{18} \text{ cm}^{-3}$) near the $[[333]]$ site: (1) Region where dislocation loops were observed; (2) region where dislocation loops were not observed.

4. Conclusion

Analysis of the results showed that the XRDS method is a highly sensitive and information valuable tool for studying early stages of solid solution decomposition in semiconductors. A review of the results relating to the methodological aspect showed that the most consistent approach is a combination of XRDS with precision lattice parameter measurements. It allows one to detect decomposition stages that cannot be visualized using TEM and to draw conclusions as to microdefect formation mechanisms.

For the GaP and InP examples, a structural microdefect formation mechanism was revealed associated with the interaction of defects forming during the decomposition and residual intrinsic defects.

The mechanism of sulfur polytypy in gallium phosphide was observed for the first time.

Study of the evolution of diffuse scattering iso-intensity contours in GaP, GaAs(Si) and Si(O) allows tracing the evolution of microdefects from matrix-coherent ones to microdefects with smeared coherency resulting from microdefect growth.

References

- Krivoglaз M.A. X-Ray and neutron diffraction in non-ideal crystals. (Eds.) V.G. Baryakhtar, M.A. Ivanov, S.C. Moss, J. Peisl. Springer, 1996: 466. <https://doi.org/10.1007/978-3-642-74291-0>
- Bublik V.T., Milvidskii M.G. Non-stoichiometry, intrinsic point defects and microdefects in $A^{III}B^V$ compounds. Pt 1. *Materialovedenie*, 1997; (2): 21–29. (In Russ.)
- Molodkin V.B., Olikhovskii S.I., Len E.G., Kyslovskyy Ye.M., Reshetnyk O.V., Vladimirova T.P., Sheludchenko B.V., Skakunova E.S., Lizunov V.V., Kochelab E.V., Fodchuk I.M., Klad'ko V.P. Dynamical theory of triple-crystal X-ray diffractometry and characterization of microdefects and strains in imperfect single crystals. *Metallofiz. Noveishie Tekhnol.*, 2016; 38(1): 99–139. <https://doi.org/10.15407/mfint.38.01.0099>
- Molodkin V.B., Olikhovskii S.I., Kyslovskyy Ye.M., Vladimirova T.P., Kochelab E.V., Reshetnyk O.V., Dovganyuk V.V., Fodchuk I.M., Lytvynchuk T.V., Klad'ko V.P., Świątek Z. X-ray diffraction characterization of microdefects in silicon crystals after high-energy electron irradiation. *Phys. status solidi (a)*, 2011; 208(11): 2552–2557. <https://doi.org/10.1002/pssa.201184253>
- Kislovskii E.N., Molodkin V.B., Olikhovskii S.I., Len E.G., Sheludchenko B.V., Lizunova S.V., Vladimirova T.P., Kochelab E.V., Reshetnik O.V., Dovganyuk V.V., Fodchuk I.M., Litvinchuk T.V., Klad'ko V.P. Combined multiparametric X-ray diffraction diagnostics of microdefects in silicon crystals after irradiation by high-energy electrons. *J. Surface Investigation. X-Ray, Synchrotron and Neutron Techniques*, 2013; 7(3): 523–530. <https://doi.org/10.1134/S1027451013030270>
- Pylypiv V.M., Vladimirova T.P., Fodchuk I.M., Ostafiychuk B.K., Kyslovskyy Ye.M., Molodkin V.B., Olikhovskii S.I., Reshetnyk O.V., Skakunova O.S., Lizunov V.V., Garpul' O.Z. Dynamical X-ray diffractometry of the defect structure of garnet crystals. *Phys. status solidi (a)*, 2011; 208(11): 2558–2562. <https://doi.org/10.1002/pssa.201184254>
- Olikhovskii S.I., Skakunova O.S., Molodkin V.B., Len' E.G., Ostafiychuk B.K., Pylypiv V.M. Simulation of reciprocal space maps for thin ion-implanted layers in yttrium-iron garnet films with defects. *Proceedings of the International Conference: Nanomaterials: Applications and Properties*. Sumy: Sumy State University, 2015; 4(1): 01PCSI05. URL: <https://essuir.sumdu.edu.ua/bitstream/123456789/42642/1/Olikhovskii.pdf>
- Sun P., Wang Y.-Q., Frost M., Schönwälder C., Levitan A.L., Mo M.-Z., Chen Z., Hastings J.B., Tynan G.R., Glenzer S.H., Heimann P. Characterization of defect clusters in ion-irradiated tungsten by X-Ray diffuse scattering. *J. Nuclear Materials*, 2018; 510: 322–330. <https://doi.org/10.1016/j.jnucmat.2018.07.062>
- Olsen R.J., Jin K., Lu C., Beland L.K., Wang L., Bei H., Specht E.D., Larson B.C. Investigation of defect clusters in ion-irradiated Ni and NiCo using diffuse X-ray scattering and electron microscopy. *J. Nuclear Materials*, 2016; 469: 153–161. <https://doi.org/10.1016/j.jnucmat.2015.11.030>
- Dederichs P.H. Effect of defect clustering on anomalous X-Ray transmission. *Phys. Rev. B*, 1970; 1(4): 1306–1317. <https://doi.org/10.1103/PhysRevB.1.1306>
- Dederichs P.H. Diffuse scattering from defect clusters near Bragg reflections. *Phys. Rev. B*, 1971; 4(4): 1041–1050. <https://doi.org/10.1103/PhysRevB.4.1041>
- Larson B.C. X-ray diffuse scattering near Bragg reflections for the study of clustered defects in crystalline materials. Ch. 9. In: R.I. Barabash, G.E. Ice, P.E.A. Turchi (Eds.), *Diffuse Scattering and the Fundamental Properties of Materials*. New York: Momentum Press, 2009: 139–160.
- Dederichs P.H. The theory of X-ray diffuse scattering and its application to the study of point defects and their clusters. *J. Phys. F: Metal. Phys.*, 1973; 3(2): 471–496. <https://doi.org/10.1088/0305-4608/3/2/010>
- Bublik V.T., Matsnev S.Yu., Shcherbachev K.D., Mezhenyi M.V., Mil'vidskii M.G., Reznik V.Ya. Diffuse X-ray scattering study of the formation of microdefects in heat-treated dislocation-free large-diameter silicon wafers. *Phys. Solid State*, 2003; 45(10): 1918–1925. <https://doi.org/10.1134/1.1620095>
- Worcester W. *Diffuznoe rasseyanie rentgenovskikh luchej v kristallakh* [Diffuse X-ray scattering in crystals. Moscow: Inostrannaya literatura, 1968, 288 p. (In Russ.)
- Datsenko L. I., Molodkin V. B., Osinovsky M. E. *Dinamicheskoe rasseyanie rentgenovskikh luchej real'nyimi kristallami* [Dynamic X-ray scattering by real crystals]. Kiev: Naukova Dumka, 1988, 198 p. (In Russ.)
- Trinkaus H. Der reflexferne Teil der diffusen Streuung von Röntgenstrahlen an Kristallen mit stark verzerrender Defekten. *Z. für Angew. Phys.*, 1971; 31: 229–235. (In German)

18. Ehrhart P., Averbach R.S. Diffuse X-ray scattering studies of neutron- and electron-irradiated Ni, Cu and dilute alloys. *Philosophical Magazine A*, 1989; 60(3): 283–306. <https://doi.org/10.1080/01418618908213863>
19. Mezheny M.V., Milvidsky M.G., Reznik V.Ya. Generation of dislocations from internal sources in heat treated dislocation-free silicon wafers under external loads. *Izvestiya Vysshikh Uchebnykh Zavedenii. Materialy Elektronnoi Tekhniki = Materials of Electronics Engineering*, 2007; (1): 11–15. (In Russ.)
20. Bublik V.T., Voronova M.I., Shcherbachev K.D., Kolin N.G., Merkurisov D.I. Structural changes in InSb single crystals irradiated by neutrons. *Izvestiya Vysshikh Uchebnykh Zavedenii. Materialy Elektronnoi Tekhniki = Materials of Electronics Engineering*, 2003; (2): 68–73. (In Russ.)
21. Bublik V.T., Voronova M.I., Shcherbachev K.D., Kolin N.G., Merkurisov D.I. Structural changes in neutrons irradiated InSb single crystals. *Izvestiya Vysshikh Uchebnykh Zavedenii. Materialy Elektronnoi Tekhniki = Materials of Electronics Engineering*, 2005; (2): 65–73. (In Russ.)
22. Bublik V.T., Voronova M.I., Shcherbachev K.D., Boiko V.M., Kolin N.G., Merkurisov D.I., Milvidskii A.M. Anomalous change in the lattice period of InP single crystals irradiated by reactor neutrons. *Izvestiya Vysshikh Uchebnykh Zavedenii. Materialy Elektronnoi Tekhniki = Materials of Electronics Engineering*, 2004; (4): 67–72. (In Russ.)
23. Bublik V.T., Voronova M.I., Shcherbachev K.D., Boiko V.M., Kolin N.G., Merkurisov D.I. The effect of reactor neutron irradiation and annealing on the structure of InP single crystals. *Izvestiya Vysshikh Uchebnykh Zavedenii. Materialy Elektronnoi Tekhniki = Materials of Electronics Engineering*, 2005; (3): 16–25. (In Russ.)
24. Filatov P.A., Bublik V.T., Shcherbachev K.D., Voronova M.I., Markova T.I. Study of microdefects in GaP and GaPZn single crystals grown by the liquid-encapsulation Czochralski method. *Crystallography Reports*, 2008; 53(2): 257–265. <https://doi.org/10.1007/s11445-008-2014-2>
25. Bublik V.T., Shcherbachev K.D., Voronova M.I., Enisherlova K.L., Rusak T.F. Diagnostics of the defects formed at different stages of intrinsic getter formation in CZ-Si. *Zavodskaya laboratoriya*, 2008; 74: 28–34. (In Russ.)